Main Manuscript for
Modeling brain signaling as Markovian helps explain its structure-function relationship

Rostam M. Razban, Anupam Banerjee, Lilianne R. Mujica-Parodi, Ivet Bahar*.
Laufer Center for Physical and Quantitative Biology, Stony Brook University, Stony Brook, NY 11794
*To whom correspondence may be addressed.
Email: bahar@laufercenter.org
Author Contributions: Paste the author contributions here.
Competing Interest Statement: Disclose any competing interests here.
Classification: Neuroscience, Physics.
Keywords: dMRI, fMRI, graph Laplacian, network neuroscience.

Abstract

Structure determines function. However, this universal theme in biology has been surprisingly difficult to observe in human brain neuroimaging data. Here, we link structure to function by hypothesizing that brain signals propagate as a Markovian process on an underlying structure. We focus on a metric called the commute time: the average number of steps for a random walker to go from region A to B and then back to A. Commute times based on white matter tracts from diffusion MRI exhibit an average ± standard deviation Spearman correlation of -0.26 ± 0.08 with functional MRI connectivity data across 434 UK Biobank individuals and -0.24 ± 0.06 across 400 HCP Young Adult brain scans. These seemingly weak correlations are stronger by a factor of 1.5 compared to communication measures such as search information and communicability for the UK Biobank individuals. The difference further widens to a factor of 5 when commute times are correlated to the principal mode of functional connectivity from its singular value decomposition. We simulate brain function and demonstrate the utility of commute time as a metric accounting for polysynaptic (indirect) connectivity to better link structure with function.

Main Text

Introduction

The brain is a network of neuronal regions (nodes) connected by white matter tracts (edges) that are stochastically organized for effective signaling (1). When tracts between regions are improperly constructed or removed, neuronal signaling will be hampered. This can lead to impaired function and thus neurological disease (2–10). Yet, despite its important role, it remains unclear how brain structure constrains its function (11, 12). Studies directly comparing connectivity matrices derived from diffusion MRI (dMRI) and functional MRI (fMRI) have found surprisingly low correlations across individuals (13, 14). dMRI measures the number of white matter tracts between brain regions (15). fMRI measures time-series of regional activity, which can be correlated to yield functional connectivities (16).

The weak relationship between structural and functional connectivity can be attributed to the two MRI-derived modalities measuring different aspects of anatomical connectivity (17). The fact that two brain regions are not directly connected by a white matter tract, does not imply a lack of functional connectivity. The path of tracts through intermediate regions connecting the two brain regions of interest influences their functional connectivity strength. Polysynaptic (indirect) connectivity goes beyond an edge-centric picture by accounting for the entire structural network of the brain (11, 18).

Metrics under the class of communication models have been developed to better capture polysynaptic connectivity (19–22). Inspired by recent results employing communication measures, we investigate whether a so far unexplored metric, commute time, can better link structure to function. Several metrics already exist for capturing polysynaptic connectivity (18). For example, communicability reweights longer

paths between nodes such that they are attenuated by the factorial of their path length (23) (Methods). This reweighting scheme allows communicability to be analytically expressed as the exponential of a reweighted connectivity matrix. However, the physical constraints underlying signaling dynamics is unclear.

Commute time is the average number of steps to randomly go back and forth between two brain regions. Applying commute time physically postulates that brain signaling propagates as a Markovian process on an underlying structure derived from dMRI (24–27). An analytical expression for commute time exists, enabling its quick calculation from the structural connectivity matrix (Methods). A few studies have already applied commute time specifically to fMRI (28, 29). We extend those works by calculating the commute time based on brain structure as derived from dMRI to investigate structural constraints in functional connectivity as derived from fMRI (**Figure 1**).

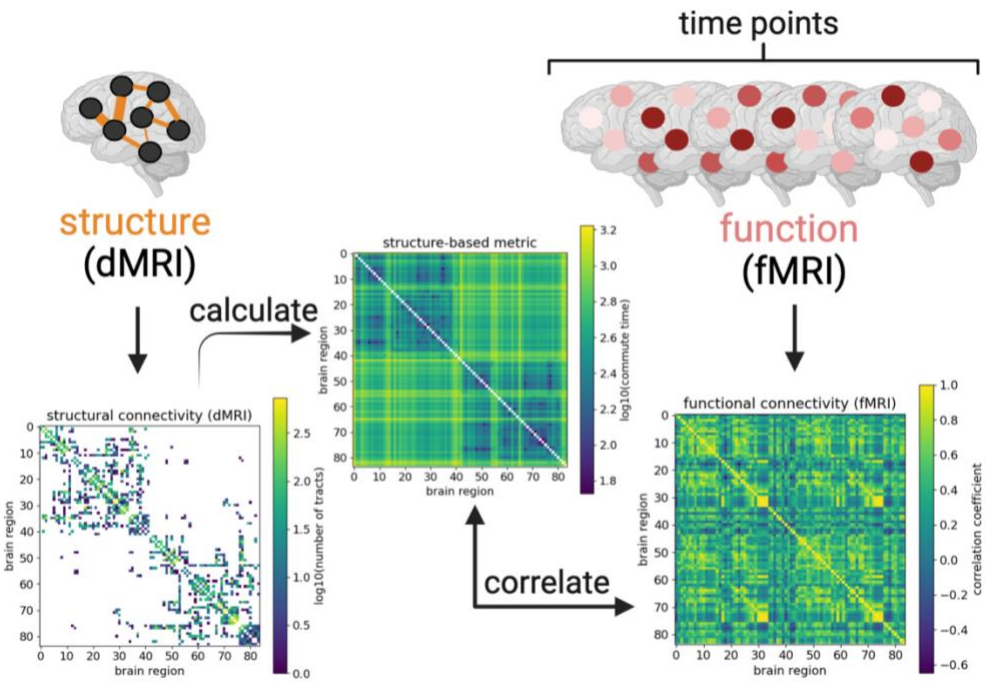

Figure 1: Bridging between brain structure and function by calculating commute time. *Connectivity matrices derived from diffusion MRI and functional MRI data are illustrated from an arbitrarily chosen UK Biobank individual (subject id: 1000366). Brighter colors reflect larger values, while structural matrix elements equal to 0 (no white matter tracts) before log transformation are colored white. Rows and columns refer to 84 brain regions from the Desikan-Killiany atlas* (30, 31)*. Brain regions are labeled such that the first half corresponds to regions in the left hemisphere; second half, right hemisphere. The sum of inverses from a rescaled form of the structural connectivity matrix (left map), yields the commute time matrix in the middle (Methods), which is then compared with correlations calculated from the fMRI time-series (right map). Figure created with biorender.com.*

Brain signaling as a Markov process

A Markov process defines state transitions based only on its current state. In other words, it has no memory of the past states that it has visited when transitioning to its next state (24, 32, 33). For a brain signal traversing from region *i* to region *j*, the process depends on all possible sequential single steps from region *i* that eventually reach region *j*, e.g. *i* to *k*, *k* to *l*, *l* to *m*, …., *z* to *j*. The Markovian metric we focus on in this paper is the commute time C_{ij}, which is defined as the average number of steps to go to and from node *i*

and an arbitrary node *j*. This can be expressed in terms of the hitting time H_{ij}, the average number of steps to go node *i* to *j*.

Equation 1

$$C_{ij} = H_{ij} + H_{ji}$$

Note that the hitting time is not generally a symmetric property, $H_{ij} \neq H_{ji}$, while the commute time is, $C_{ij} = C_{ji}$. Because structural and functional connectivity matrices derived from dMRI and fMRI are symmetric, we focus on C_{ij}, rather than H_{ij}.

To derive an analytical expression for C_{ij}, we first need an expression for H_{ij}. We start by writing down a self-consistent equation for H_{ij}. Assume that we take one step away from node *i* to any node *k* on route to node *j.* The hitting time H_{ij} can be updated in terms of H_{kj} as follows,

Equation 2

$$H_{ij} = \sum_{k}^{N} M_{ik}\left(1 + H_{kj}\right)$$

There are *N* total nodes in the network. The symbol ***M*** corresponds to the transition matrix and can be expressed as $\boldsymbol{M} = \boldsymbol{AD}^{-1}$, where ***A*** is the adjacency matrix and ***D*** is a diagonal matrix with nodes' degrees along the diagonal. Because the probability of taking a step to another node *k* only depends on the possible transitions from the current node *i*, Equation 2 corresponds to a Markov process.

Throughout this paper, we use weighted graphs because dMRI tractography provides the number of streamline counts of white matter tracts between two brain regions. Thus, ***A*** is a weighted adjacency matrix and the diagonal elements in ***D*** are equal to the sum of weights for that particular node, i.e.

Equation 3

$$D_{ii} = \sum_{j}^{N} A_{ij}$$

Note that the weighted adjacency matrix is equivalent to the structural connectivity matrix. We use the words adjacency and structural connectivity interchangeably throughout the text.

The probability of taking a step from brain region *i* to *j*, M_{ik}, is proportional to the number of tracts derived from dMRI. Thus, Equation 2 can be simplified because the sum of the transition matrix ***M*** across any row or column equals to 1. We further simplify by also re-expressing Equation 2 in terms of the Laplacian matrix $\boldsymbol{\Gamma} = \boldsymbol{D} - \boldsymbol{A}$. Skipping steps outlined in the Methods, we can then solve for H_{ij}.

Equation 4

$$H_{ij} = \sum_{k}^{N}\left([\Gamma^{-1}]_{ik} - [\Gamma^{-1}]_{ji} - [\Gamma^{-1}]_{jk} + [\Gamma^{-1}]_{jj}\right) D_{kk}$$

Inserting Equation 4 into Equation 1, we now have an analytical expression for commute time C_{ij}.

Equation 5

$$C_{ij} = \left([\Gamma^{-1}]_{ii} + [\Gamma^{-1}]_{jj} - 2[\Gamma^{-1}]_{ij}\right) \sum_{k}^{N} D_{kk}$$

The exact same expression for C_{ij} in Equation 5 has been previously derived elsewhere (24, 26). Nonetheless, we check the accuracy of the final expression for C_{ij} by comparing it to its numerical solution. We numerically determine all possible C_{ij} for an arbitrarily chosen UK Biobank individual's dMRI

derived structural connectivity matrix. We find excellent agreement between theoretically and numerically calculated commute times across all brain region pairs (Figure S1).

Thus, we procced to repeatedly evaluate Equation 5 across all possible pairs of brain regions for a given individual and investigate whether this Markovian property can help bridge between structural and functional connectivities.

Results

Commute time captures simulated function

We first aim to establish that commute times can in principle capture correlations of time-series data, also called functional connectivities, among all possible pairs of nodes. To this aim, we arbitrarily select an individual from the UK Biobank (subject id: 1000366). We process their dMRI data to derive a structural connectivity matrix of white matter tracts under the Desikan-Killiany atlas (84 brain regions) (30, 31). From the structural connectivity matrix, the Laplacian matrix is constructed and its mathematical inverse is taken to compute the commute time (Equation 5).

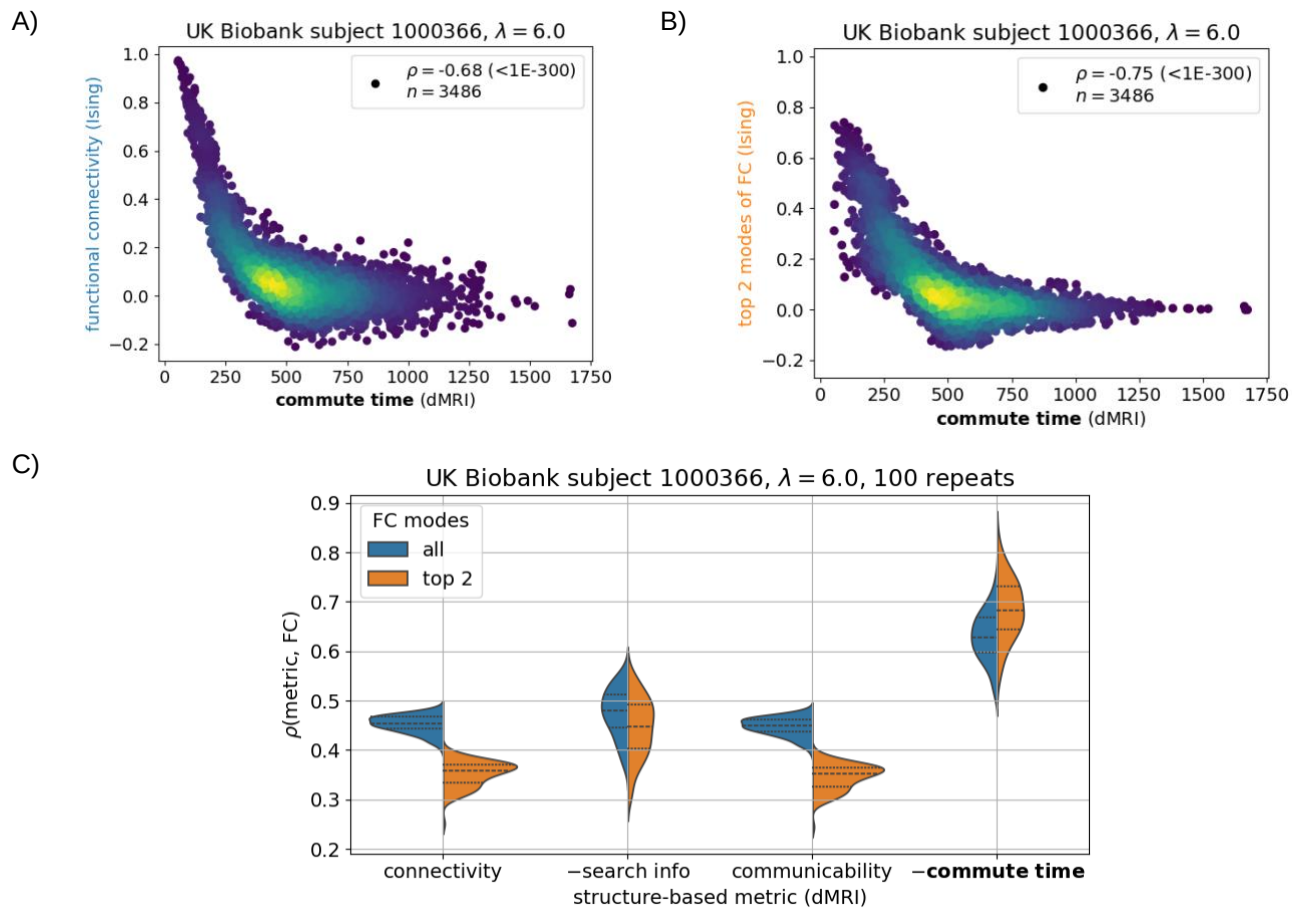

Figure 2: Commute time captures functional connectivity in a mean-field Ising simulation. *The Ising simulation with a coupling strength λ = 6.0 is run on a dMRI-derived structure from an arbitrary UK Biobank individual (subject id: 1000366) under the Desikan-Killiany atlas (84 brain regions). A) and B) Data points correspond to all possible pairs of brain regions (n = 84x83/2) and are colored to capture the density of points, with brighter colors corresponding to greater density. The entirety of the functional connectivity matrix (FC) is considered in A). Only the top two modes of the FC matrix are considered in B). The symbol ρ corresponds to the Spearman correlation coefficient with its p-value following in parenthesis. C) Commute time exhibits a stronger correlation with simulated functional connectivity compared to three other metrics (along the abscissa). One-hundred*

replicate Ising simulations are run. For visualization purposes, the additive inverse (–) of search information and commute time are taken such that all structure-based metrics are positively correlated with FC. Each metric yields two distributions, where the orange distribution only includes the top two modes of the FC matrix. The dashed lines within the distribution correspond to its quartiles: 25th percentile, 50th percentile (median) and 75% percentile. Corresponding Kolmogorov-Smirnov pairwise tests between metrics are summarized in Table S2.

Functional connectivities (FCs) in this subsection are generated by iteratively simulating a mean-field Ising system composed of 84 up or down spins with a single coupling strength parameter λ (Methods, **Figure 5**). The structural connectivity of the Ising system is set to the same UK Biobank individual. We choose to simulate a mean-field Ising system because of its simplicity (only one parameter which can be uniquely fitted to the data) and previous results demonstrating its utility in capturing global brain dynamics (34, 35). The generated time-series are corelated with each other to create the corresponding FC matrix. Results are presented in **Figure 2**. In the Supplement, we corroborate our results with the Wilson-Cowan model (36, 37), a more complicated (24 parameters, Table S1) and realistic simulation of brain function (Figure S2).

Figure 2A demonstrates that commute times based on dMRI significantly captures functional connectivity from the Ising simulation for an arbitrarily chosen UK Biobank individual. The commute time-FC Spearman correlation coefficient (ρ) is -0.66 with a p-value (p) < 10^{-300}. Larger commute times yield smaller functional connectivities because the two regions are separated by a larger number of intermediate steps, making the two regions' signaling more likely to be uncorrelated. FC values may be influenced by many other factors besides structure. To potentially minimize noise and enrich its structural signature, we decompose the FC matrix into its eigenmodes and only compare its top two modes to commute time in **Figure 2B**. The comparison to commute time yields a stronger correlation (ρ = -0.72, p < 10^{-300}). Notably, the correlation is not as strong as if we compare FC's top mode to commute time because edges begin separating into distinct clusters (Figure S3).

We further investigate how the structure-function relationship is affected by the Ising model's single parameter, the coupling strength λ. When the coupling strength increases, a larger structure-function correlation is observed on average (Figure S4). Young adults' brains have been shown to have coupling strengths just below the Ising model critical point that further decrease with age (35). This roughly corresponds to the coupling strength value presented in **Figure 2**. Similar weakening in the structure-function relationship is seen for the Wilson-Cowan model when the coupling constant is decreased (Figure S5).

To ensure that our results are not an artifact of the particular individual's brain structure on which function is simulated, we present results for several other individuals' brain structures in the Supplement (Figure S6). We also assess commute time's performance with respect to other communication measures and demonstrate that commute time yields a stronger structure-function correlation compared to communicability and search information (**Figure 2C**). In summary, the observed correlation between structure-dependent commute times and functional connectivity (as deduced from simulations on the same structure) confirms the utility of adopting commute time as a metric to correlate with fMRI-derived functional connectivity.

Commute time better captures brain function

With the encouraging results from simulations of brain function, we proceed to compare the commute times to FCs from fMRI for the same individual, where both modalities are processed according to the same Desikan-Killiany atlas (Methods). **Figure 3A** and **B** illustrate the results for the same arbitrarily selected UK Biobank individual in the previous subsection. A statistically significant (p = $4.0*10^{-44}$) but weak correlation of -0.23 is observed across all possible pairs of brain regions. This correlation becomes stronger when only including FC's top mode (ρ = -0.28, p = $7.8*10^{-63}$). We do not need to include the top two modes as in the Ising simulation (**Figure 2B**) because the top eigenvalue in fMRI's FC is much larger than its second largest eigenvalue (Figure S7). Compared to simulated FCs in the previous subsection, the correlation between commute time and fMRI-derived FC is much weaker. One reason is that the fMRI FC matrix deviates from

the dMRI structural connectivity matrix much more than that of the simulated FC (Figure S8). The purpose of commute time is to bridge the gap between structural connectivity and FC matrices. However, based on obtained correlation coefficients, the gap is still too large. We will return to this point in the Discussion by separately studying intra-hemispheric connections and artificially introducing homotopic connections.

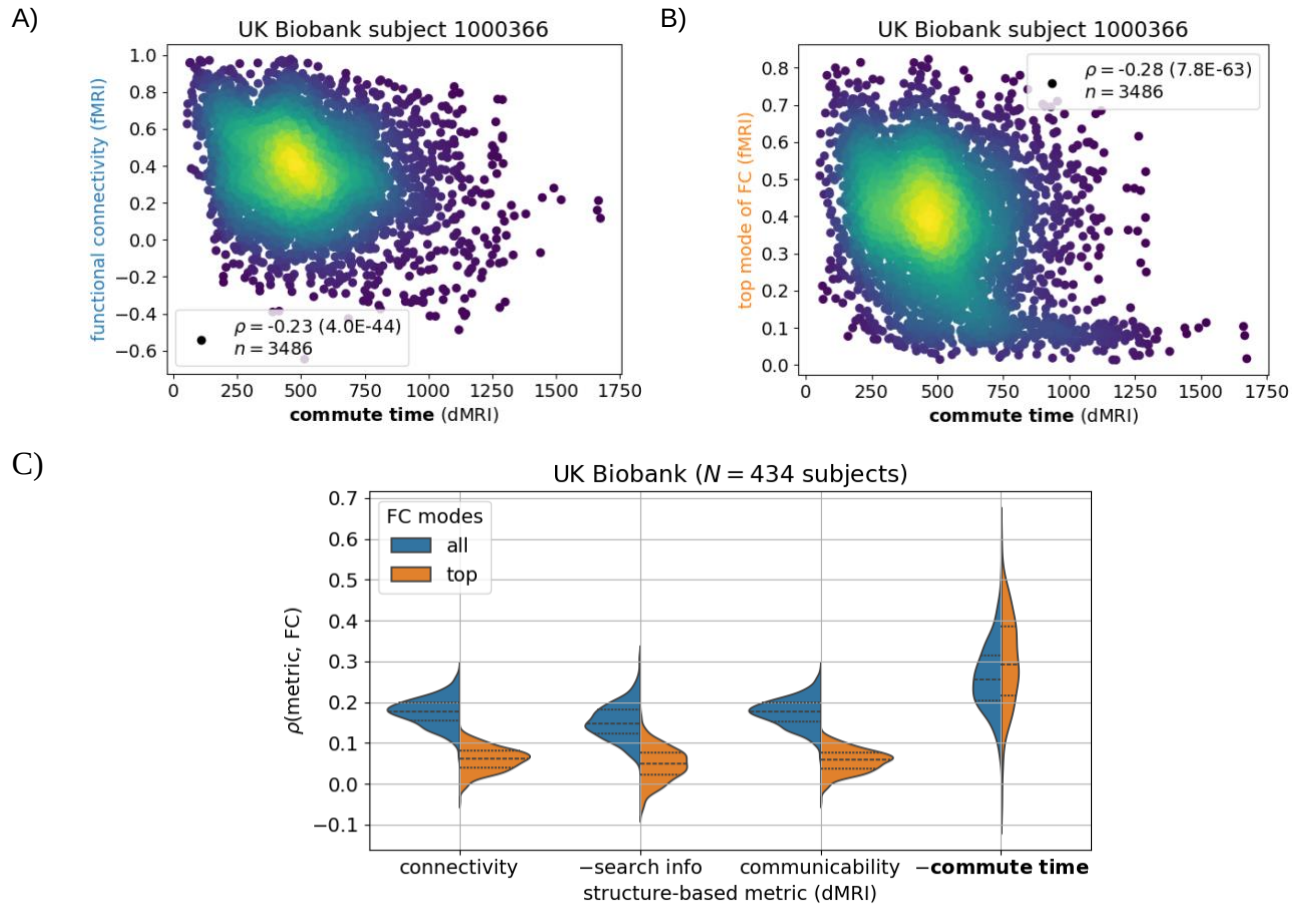

Figure 3: Commute time marginally captures functional connectivity from functional MRI across the UK Biobank. *fMRI and dMRI data are processed according to the Desikan-Killiany atlas (84 brain regions). A) and B) Data points correspond to all possible pairs of brain regions (n = 84x83/2) and are colored to capture the density of points, with brighter colors corresponding to greater density. The entirety of the functional connectivity matrix (FC) is considered in A). Only the top mode of the FC matrix is considered in B). The symbol ρ corresponds to the Spearman correlation coefficient with its p-value following in parenthesis. C) Commute time exhibits a stronger correlation with FC compared to three other metrics (along the abscissa). Each metric has two plotted distributions, where the orange distribution only includes the top mode of the FC matrix. Corresponding Kolmogorov-Smirnov pairwise tests between metrics are summarized in Table S3. N corresponds to the number of human subjects considered from the UK Biobank.*

We extend our analysis to 434 UK Biobank subjects for which we have access to their dMRI and fMRI data and plot the distribution of correlation coefficients. An average ± standard deviation commute time-FC correlation of -0.26 ± 0.082 is observed between commute time and functional connectivity (**Figure 3C**, blue distribution), which rises to -0.30 ± 0.11 when only including the top mode of FC (**Figure 3C**, orange distribution). To place the average correlation value of -0.26 into context, we compare commute time's results to the dMRI-derived structural connectivity as a control, and two leading communication metrics in the field: search information and communicability (18). We find that commute time yields a stronger structure-function correlation than the other three structural metrics (**Figure 3C**). Moreover, when only including the top mode of FC, the difference between the metrics widens (Kolmogorov-Smirnov test statistic (KS) = 0.59 vs 0.95 (Table S3)). This is because structural connectivity, search information and communicability predict FC's top mode more poorly than the entire FC across UK Biobank individuals

(compare corresponding orange vs. blue distributions in **Figure 3C**). This hints that these metrics may be capturing nonstructural drivers of FC, since FC's top mode corresponds more strongly to structural constraints as indicated by simulation results in the previous subsection.

To ensure that our results are not sensitive to the particular atlas choice for dMRI and fMRI processing, we present results according to the finer Talairach atlas (38). Figure S9 shows that commute time again outperforms other metrics; however, the correlations are lower across the board. This is consistent with a previous result in the literature showing that atlases delineating more brain regions yield smaller structure-function correlations (13) (see (39) for an exception). To further corroborate our results, we examine dMRI and fMRI from the Human Connectome Project (HCP) Young Adult dataset (17, 40). We investigate the HCP Young Adult 100 Unrelated Subjects subset and find similar trends as in **Figure 3C** (Figure S10). These correlations are slightly weaker compared to those for the UK Biobank. Yet, commute time still outperforms all other metrics with a correlation of -0.24 ± 0.060; further rising to -0.25 ± 0.084 when only correlating with FC's top mode.

Structure-function strength weakly relates to biomarkers

Commute time outperforms other metrics at predicting function on average, however, there is a large range across individuals with correlations ranging from 0.059 to 0.58 and from –0.053 to 0.61 when focusing on FC's top mode for the UK Biobank (**Figure 3C**). We investigate whether commute time-FC correlations are systemically weaker for individuals in the UK Biobank with mental health disorders or neurological diseases, as defined by the International Classification of Diseases-10 codes F and G, respectively (41). We found small differences, regardless of whether the top mode of FC is used (**Figure 4A**). Individuals with mental disorders have slightly weaker commute time-FC correlations compared to healthy individuals that is not statistically significant (KS = 0.55, p = 0.12 (Table S4)); however, the sample size of individuals with mental disorders is small (only 4 individuals). Interestingly, individuals diagnosed with neurological/brain diseases display structure-function correlations similar to healthy individuals in the UK Biobank. These results are surprising because mental health disorders are normally diagnosed by behavior, while neurological diseases have a clearer connection to brain structure. For example, a stroke leads to neuronal loss which reroutes signal transmission (5, 42, 43). However, our preliminary results indicate that mental health disorders may be just as vulnerable to impaired structure-function relationships, if not more.

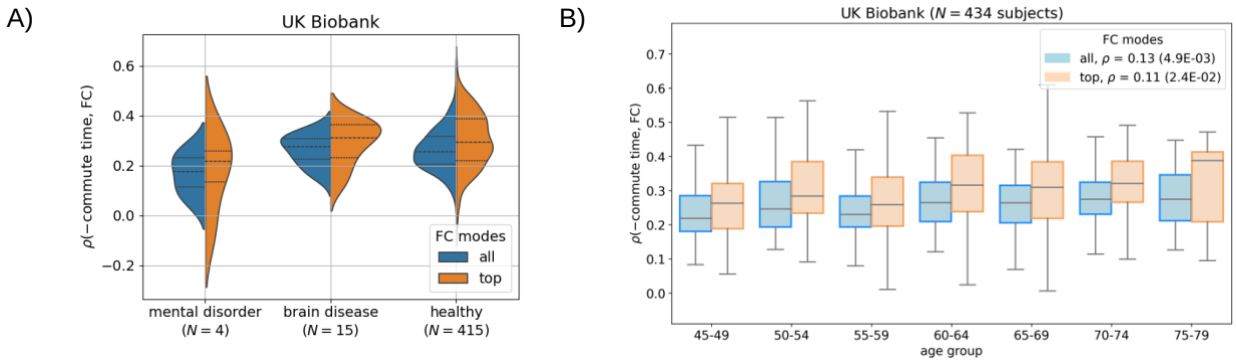

Figure 4: The strength of the commute time-functional connectivity relationship demonstrates weak pathological significance. *fMRI and dMRI data are processed according to the Desikan-Killiany atlas throughout (84 brain regions). A) Small differences are seen between individuals with brain disorders and diseases compared to healthy individuals in the UK Biobank. None of the corresponding Kolmogorov-Smirnov pairwise tests between groups are significant (Table S4). B) Older brains have slightly stronger correlations between commute time and functional connectivity (FC). Two distributions are plotted, where the orange distribution only includes the top mode of the FC matrix. The symbol ρ corresponds to the Spearman correlation coefficient with its p-value in parenthesis, calculated for all data points. The symbol N refers to the number of human individuals from the UK Biobank.*

We proceed to test whether aging results in a breakdown in the relationship between brain structure and function. This has been shown to be the case with other metrics (22) and might be expected because older brains have been inferred to have lower connection strengths between regions (35). In **Figure 4B**, we

surprisingly find that the magnitude of the commute time-FC correlation slightly increases with age. In other words, older brains have a stronger structure-function relationship. This relationship slightly weakens when only the top mode is considered, indicating greater robustness to aging. Our strengthening aging trends contrast with recent results finding that among 40 different predictors (does not include commute time), the correlation of the best predictor for a given individual decreases with age (22). This contrasting result highlights the importance of metric choice in making statements about brain-wide aging trends.

We are not able to corroborate our aging findings with the HCP Young Adult dataset. When looking at four age groups, we find minimal differences in the distributions of commute time-FC correlations (Figure S11). The lack of any aging trends in this dataset may be due to the narrow range compared to the UK Biobank, 22-36 compared to 46-79 years old (Table S7). We also analyzed Mini-Mental State Examination scores collected by the HCP Young Adult to gauge whether the structure-function correlation underlies cognition and found minimal differences (Figure S12). Finally, as a control, we confirm that sex does not confound the relationship between commute time and FC (Figure S13).

Discussion

We build upon communication metrics' recent successes at capturing brain dynamics by investigating whether commute times calculated along structures determined by dMRI can capture functional connectivities. We demonstrate that commute time outperforms other metrics such as communicability because commute time physically calculates the random diffusion of brain signals across its structure based on Markovian dynamics. Longer paths are not arbitrarily down-weighted as in communicability. Moreover, including the physical length of connections as done by the search information metric does not satisfactorily address the problem of linking structure to function. Many studies only consider intra-hemisphere white matter tracts in their data analysis (18, 19), because dMRI is known to be less accurate in reconstructing longer tracts (44, 45). Commute time still outperforms other metrics when only analyzing intra-hemisphere tracts from the left-hemisphere (Figure S14). The resulting average correlation coefficient increases to –0.31 ± 0.11 across the 434 UK Biobank individuals, demonstrating that commute times better account for intra-hemisphere FCs. To check whether results are dependent on the tractography method used to analyze the dMRI data, we performed probabilistic tractography and found similar trends (Figure S15). We also corroborated our findings with publicly available probabilistic tractography data from a recent study on HCP Young Adult (Figure S16).

In addition to better performance, commute time has several advantageous properties that neither communicability nor search information simultaneously both have. As with communicability, commute time has an analytical expression. As with search information, commute time can distinguish between pairs of regions with no tracts. All three structure-based metrics have no fitted parameters. Nonetheless, commute time still does not strongly link structure to function, given that the commute time-FC Spearman correlation is on average -0.26 ± 0.08 across 434 UK Biobank individuals. The main challenge is that structural connectivity matrices are sparse, while FC matrices are dense (11, 14). Commute time helps transform structural connectivity matrices to become denser; however, it still pales in comparison to FC matrices (**Figure 1**). Particularly noticeable are the strong homotopic connections present in FC, but not in the structural connectivity or commute time matrix. Homotopic connections correspond to interhemispheric connections between the same functional brain region across the two hemispheres (diagonal elements on the two off-diagonal quadrants in **Figure 1**) and have been previously shown to be some of the most stable functional connections (14, 39, 46, 47). In an attempt to better capture FC, we manually introduce homotopic tracts in the structural connectivity matrices. Overall, we find marginal improvements in the commute time-FC correlation when 100 tracts are added to each possible homotopic pair for individuals in the HCP Young Adult dataset (-0.30 ± 0.08 vs -0.24 ± 0.06 as shown in Figure S17 vs Figure S10). We investigate the correlation strength when treating the number of added homotopic tracts as a parameter and find that improvements level off at around 1,000 added tracts. Compared to randomly added tracts, homotopic added tracts improve commute time-FC correlations. The difference becomes especially pronounced as more tracts are added (Figure S18).

A slight Increase is seen when only correlating commute time to the top mode of FC, -0.30 ± 0.11; however, we are still a ways away from accurately predicting FC from structure (**Figure 3C**). Clearly, other factors besides structure dictate brain function, such as neurotransmitter expression and the connection directionality, factors that dMRI and fMRI do not capture (11). We attempt to enrich for structural signatures by taking the top mode of FC, which we verify with simulations (**Figure 2B**). It is interesting to note that other structure-based metrics yield weaker structure-function correlations with the top mode of FC, indicating that they capture other effects besides structural signatures in FC (**Figure 2C**).

Results investigating the pathological implications of a weak commute time-FC correlation are inconclusive because of small sample sizes. In the main text, we only have access to 434 UK Biobank individuals, 4 and 15 of which have been diagnosed with a mental health disorder and/or neurological disease, respectively. In future studies, we will obtain access to more UK Biobank dMRI and fMRI scans to more thoroughly investigate the intersection between brain structure and function with disease. Intriguingly, we already find that older individuals have slightly stronger structure-function relationships than younger people. White matter is one of the last brain areas to fully develop in young adulthood (48) and our results suggest that its continued maturation in advanced ages could lead to a stronger coupling with function.

Materials and Methods

Commute time

We expand upon the main text's derivation for H_{ij} by filling in the gaps between Equation 2 to Equation 4. We can simplify **Error! Reference source not found.** by noting that the sum of the transition matrix ***M*** for a ny row or column equals to 1.

Equation 6

$$\begin{aligned} H_{ij} &= \sum_{k}^{N} M_{ik} + \sum_{k,k\neq j}^{N} M_{ik} H_{kj} \\ &= 1 + \sum_{k,k\neq j}^{N} M_{ik} H_{kj} \end{aligned}$$

Next, we write Equation 6 in matrix notation by defining matrices with a ^ symbol, designating that the jth element from row vectors and j^{th} columns and rows from ***M*** are removed from consideration.

Equation 7

$$\widehat{\boldsymbol{H}}_j = \widehat{\mathbf{1}}^T + \widehat{\boldsymbol{H}}_j \widehat{\boldsymbol{M}}$$

Note that $\widehat{\boldsymbol{H}}_j$ is a 1 x (*N*-1) row vector and $\widehat{\boldsymbol{M}}$ is a (*N*-1) x (*N*-1) matrix. We can simplify the expression and solve for $\widehat{\boldsymbol{H}}_j$ by expanding the transition matrix $\widehat{\boldsymbol{M}}$ in terms of the Laplacian matrix ***Γ = D – A***.

Equation 8

$$\begin{aligned} \widehat{\boldsymbol{H}}_j &= \widehat{\mathbf{1}}^T + \widehat{\boldsymbol{H}}_j \widehat{\boldsymbol{A}} \widehat{\boldsymbol{D}}^{-1} \\ \widehat{\boldsymbol{H}}_j &= \widehat{\mathbf{1}}^T + \widehat{\boldsymbol{H}}_j \left(\widehat{\boldsymbol{D}} - \widehat{\boldsymbol{\Gamma}}\right) \widehat{\boldsymbol{D}}^{-1} \\ \widehat{\boldsymbol{H}}_j &= \widehat{\mathbf{1}}^T + \widehat{\boldsymbol{H}}_j - \widehat{\boldsymbol{H}}_j \widehat{\boldsymbol{\Gamma}} \widehat{\boldsymbol{D}}^{-1} \\ \rightarrow \widehat{\boldsymbol{H}}_j &= \widehat{\mathbf{1}}^T \widehat{\boldsymbol{D}} \widehat{\boldsymbol{\Gamma}}^{-1} \end{aligned}$$

The final form of Equation 8 can be written back in terms of components as,

Equation 9

$$H_{ij} = \sum_{k,k\neq j}^{N} \left[\hat{\Gamma}^{-1}\right]_{ik} \hat{D}_{kk}$$

In the Supplement, we demonstrate how we can express $\hat{\boldsymbol{\Gamma}}^{-1}$ in terms of $\boldsymbol{\Gamma}^{-1}$ by sequentially adding one row and then one column to $\hat{\boldsymbol{\Gamma}}^{-1}$. We utilize Greville's formula twice to calculate the updated matrix inverses (49, 50). Below is the result,

Equation 10

$$\begin{aligned} H_{ij} &= \sum_{k,k\neq j}^{N} \left([\Gamma^{-1}]_{ik} - [\Gamma^{-1}]_{ji} - [\Gamma^{-1}]_{jk} + [\Gamma^{-1}]_{jj}\right) \hat{D}_{kk} \\ &= \sum_{k}^{N} \left([\Gamma^{-1}]_{ik} - [\Gamma^{-1}]_{ji} - [\Gamma^{-1}]_{jk} + [\Gamma^{-1}]_{jj}\right) D_{kk} \end{aligned}$$

The final expression in Equation 10 is equivalent to Equation 4 in the main text. Commute time can then be obtained by summing H_{ij} and H_{ji} (Equation 5).

Commute time (C_{ij}) is closely related to other physical properties besides random walks. The mean-squared fluctuations in internal distances ($\langle \Delta R_i \Delta R_j \rangle$) of a network of nodes connected by springs, called the Elastic Network Model (51, 52), is proportional to commute time (24, 32). The resistance distance (Ω_{ij}) between two nodes in an electrical network is also proportional to commute time (26, 53, 54). $\langle \Delta R_i \Delta R_j \rangle$ and Ω_{ij} have independent derivations based in statistical mechanics and electromagnetism, respectively.

Equation 11

$$\langle \Delta R_i \Delta R_j \rangle \propto \Omega_{ij} \propto c_{ij} \propto [\Gamma^{-1}]_{ii} + [\Gamma^{-1}]_{jj} - 2[\Gamma^{-1}]_{ij}$$

Commute time is the most relevant property in the current application because its basis in the Markovian propagation of signals provides a physical mechanism for brain signaling.

Communicability

Communicability (CMY) is analytically expressed in terms of the graph's weighted adjacency matrix (**A**) (23, 55, 56).

Equation 12

$$CMY(i,j) = \sum_{n=0}^{\infty} \frac{1}{n!} \left(\frac{A_{ij}}{\sqrt{D_{ii}D_{jj}}}\right)^n = \exp\left[\frac{A_{ij}}{\sqrt{D_{ii}D_{jj}}}\right]$$

The weighted adjacency matrix is normalized based on the total number of tracts for a node *i*, D_{ii} (Equation 3). By scaling by the factorial of the path length, the summation can be exactly expressed as an exponential. This factorial factor can physically correspond to springs on a surface plane (23). However, it is unclear how the physical movement of springs in space corresponds to brain signaling along its structure.

Search Information

Search information (SI) is the amount of information in bits that a random walk needs in order to follow the shortest path based on tract lengths (19, 57). It is expressed in terms of the transition matrix **M**, which

can be computed in terms of the weighted adjacency matrix as noted in the main text when deriving commute time.

Equation 13

$$SI(i,j) = \log_2\left[M_{ia}M_{ab}M_{bc} * \ldots * M_{zj}\right]$$

The nodes ***a, b, …, z*** are located on the shortest path connecting node *I* to node *j*. We calculate search information using previously published code in the Brain Connectivity Toolbox (58). ChatGPT was used to help translate the original Matlab code into Python.

Ising simulation of brain function

The following steps are performed to generate the functional connectivity (FC) matrix from the Ising model.

1. Set the static structure based on an individual's dMRI data. Edges are assigned weights A_{ij} corresponding to the number of white matter tracts observed between pairs of regions in diffusion MRI.
2. Set the global coupling strength λ for all edges. λ is the only parameter in the Ising simulation and dictates the energy of the system, $E = -\lambda \sum_{ij} A_{ij} s_i s_j$, where s_i corresponds to the spin state of region *i* and can either be +1 or -1. The larger the λ, the more likely that all nodes will be all up or all down. For smaller λ, entropy wins out and individual spins are equally likely to be up or down regardless of the states of their connected neighbors.
3. Initialize the simulation by randomly assigning spins of +1 or -1 to each of the nodes.
4. Evolve the simulation by one timestep by randomly attempting to flip 15% of the nodes' spins. We accept attempted sets of spin flips according to the Metropolis-Hastings algorithm (59), which more likely accepts spin flips that lower the system's energy while obeying detailed balance. The exact number of randomly attempted spin flips for a certain number of iterations does not matter so long as the simulation is in the equilibrium regime.
5. Repeat step 4) for a total of 5000 times to ensure that the state space is well-sampled.
6. Convolute the Ising spins with the Volterra kernel hemodynamic response function (60) to output a fMRI BOLD-like signal.
7. Correlate the entire time-series across pairs of regions to create the FC matrix.

Figure 5 shows a schematic of the Ising simulation for a system with seven nodes and one spin flip attempted per timestep.

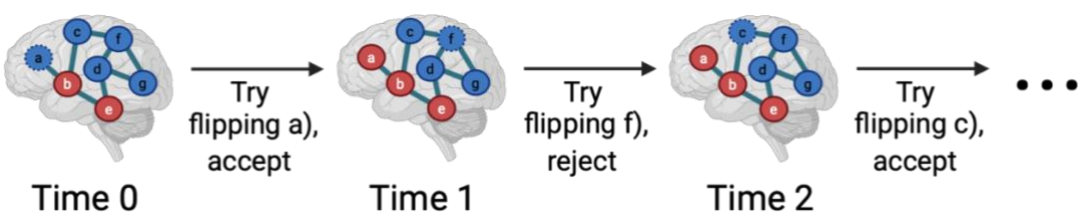

Figure 5: Schematic of the Ising simulation evolving in time. *We start with a fixed structure whose spins are randomly initialized either up (blue) or down (red) at time 0. We then randomly choose a node and attempt to flip its spin. At time 0, we attempt to flip node a). It is accepted according to the Metropolis-Hastings algorithm because the energy becomes stabilized by λ units. At time 1, we attempt to flip node f). Because the energy is destabilized by 3*λ, we accept it with a probability of* $e^{-3\lambda}$ *according to the Metropolis-Hastings algorithm. In the figure, this particular realization of f)'s spin flip is rejected. At time 2, we attempt to flip node c). The change in energy is 0, so we accept the spin flip. This schematic is simplified such that all edges have the same weight. The simulation also accounts for the number of tracts for each edge derived from the diffusion MRI of an arbitrarily chosen individual. Figure created with biorender.com.*

dMRI processing

We take preprocessed dMRI scans from the UK Biobank (61) and calculate connectivity matrices using the Diffusion Imaging in Python software (31). For each individual, we determine the number of streamline counts of white matter tracts between regions and their average lengths. We input the Desikan-Killiany atlas (30, 31) to distinguish between white and neuronal regions in the gray matter. We perform deterministic tractography and reconstruct the orientation distribution function using the Constant Solid Angle (Q-Ball) method with a spherical harmonic order of 6 (62). The relative peak threshold is set to 0.8 with a minimum separation angle of 45°. We only seed voxels in the white matter and count tracts that end in the gray matter. Minimum step size of tracts is 0.5 mm. Self-loops are removed from consideration such that all diagonal elements in the structural connectivity matrix are equal to 0.

To make sure results are not an artefact of the particular brain atlas, we also process dMRI scans according to the Talairach atlas (38). Regions that have zero inferred white matter tracts are removed from consideration. For some individuals, different regions are removed from consideration. The average number of nodes per individual is 727 (63).

To make sure results are not an artefact of the tractography method, we also perform probabilistic tractography and reconstruct the orientation distribution function using the same Constant Solid Angle (Q-Ball) method with a spherical harmonic order of 6.

The same procedure is applied to the HCP Young Adult dataset from accessed preprocessed dMRI (64, 65) to generate the structural connectivity matrices. Demographic details for both the HCP Young Adult and UK Biobank dataset can be found in Table S7.

fMRI processing

We take preprocessed fMRI scans from the UK Biobank (66). The cleaned, voxel space time series are band-pass filtered to only include neuronal frequencies (0.01 to 0.1 Hz) and smoothed at a full width at half maximum of 5 mm. Finally, we parcellate into 84 brain regions of interest according to the Desikan-Killiany atlas (30, 31), the same as in dMRI processing. We also process fMRI scans according to the Talairach atlas (38) and remove from consideration those brain regions that have no white matter tracts (see dMRI processing). Functional connectivity is calculated by correlating the entire processed time-series between brain regions according to the Pearson correlation coefficient.

The same procedure Is applied to the HCP Young Adult dataset from accessed preprocessed fMRI (64) to generate the functional connectivity matrices. Acquisition details such as field strength and repetition time for both datasets can be found in Table S8.

Data Availability

Scripts necessary to reproduce figures and conclusions reached in the text can be found at github.com/rrazban/brain_commute. Please refer to the respective UK Biobank (ukbiobank.ac.uk) and HCP Young Adult website (db.humanconnectome.org) to access previously published dMRI and fMRI data (40, 61).

Acknowledgments

We would like to thank Botond Antal for sharing his fMRI expertise and sharing his Wilson-Cowan Python function wrappers on the Virtual Brain. We would also like to thank Mobolaji Williams for theoretical support on deriving the analytical expression for commute time.

This research has been conducted using the UK Biobank Resource under Application Number 37462.

Data were provided in part by the Human Connectome Project, WU-Minn Consortium (Principal Investigators: David Van Essen and Kamil Ugurbil; 1U54MH091657) funded by the 16 NIH Institutes and Centers that support the NIH Blueprint for Neuroscience Research; and by the McDonnell Center for Systems Neuroscience at Washington University.

References

1. D. S. Bassett, O. Sporns, Network neuroscience. *Nat. Neurosci.* **20**, 353–364 (2017).

2. W. W. Seeley, R. K. Crawford, J. Zhou, B. L. Miller, M. D. Greicius, Neurodegenerative Diseases Target Large-Scale Human Brain Networks. *Neuron* **62**, 42–52 (2009).

3. A. Fornito, A. Zalesky, M. Breakspear, The connectomics of brain disorders. *Nat. Rev. Neurosci.* **16**, 159–172 (2015).

4. A. Fornito, E. T. Bullmore, Connectomics: A new paradigm for understanding brain disease. *Eur. Neuropsychopharmacol.* **25**, 733–748 (2015).

5. A. Raj, F. Powell, Models of Network Spread and Network Degeneration in Brain Disorders. *Biol. Psychiatry Cogn. Neurosci. Neuroimaging* **3**, 788–797 (2018).

6. D. S. Bassett, E. T. Bullmore, Human brain networks in health and disease. *Curr. Opin. Neurol.* **22**, 340–347 (2009).

7. G. Deco, M. L. Kringelbach, Great expectations: Using whole-brain computational connectomics for understanding neuropsychiatric disorders. *Neuron* **84**, 892–905 (2014).

8. S. E. Morgan, S. R. White, E. T. Bullmore, P. E. Vértes, A network neuroscience approach to typical and atypical brain development. *Biol. Psychiatry Cogn. Neurosci. Neuroimaging* **3**, 754–766 (2018).

9. A. Perry, G. Roberts, P. B. Mitchell, M. Breakspear, Connectomics of bipolar disorder: a critical review, and evidence for dynamic instabilities within interoceptive networks. *Mol. Psychiatry* **24**, 1296–1318 (2019).

10. X. Bu, M. Cao, X. Huang, Y. He, The structural connectome in ADHD. *Psychoradiology* **1**, 257–271 (2021).

11. L. E. Suárez, R. D. Markello, R. F. Betzel, B. Misic, Linking Structure and Function in Macroscale Brain Networks. *Trends Cogn. Sci.* **24**, 302–315 (2020).

12. C. J. Honey, J. P. Thivierge, O. Sporns, Can structure predict function in the human brain? *Neuroimage* **52**, 766–776 (2010).

13. C. J. Honey, *et al.*, Predicting human resting-state functional connectivity from structural connectivity. *Proc. Natl. Acad. Sci. U. S. A.* **106**, 2035–2040 (2009).

14. B. Q. Rosen, E. Halgren, A whole-cortex probabilistic diffusion tractography connectome. *eNeuro* **8**, 1–21 (2021).

15. D. K. Jones, T. R. Knösche, R. Turner, White matter integrity, fiber count, and other fallacies: The do's and don'ts of diffusion MRI. *Neuroimage* **73**, 239–254 (2013).

16. J. Yang, S. Gohel, B. Vachha, Current methods and new directions in resting state fMRI. *Clin. Imaging* **65**, 47–53 (2020).

17. J. S. Elam, *et al.*, The Human Connectome Project: A retrospective. *Neuroimage* **244**, 118543 (2021).

18. C. Seguin, O. Sporns, A. Zalesky, Brain network communication: concepts, models and applications. *Nat. Rev. Neurosci.* **24**, 557–574 (2023).

19. J. Goni, *et al.*, Resting-brain functional connectivity predicted by analytic measures of network communication. *Proc. Natl. Acad. Sci. U. S. A.* **111**, 833–838 (2014).

20. A. Avena-Koenigsberger, *et al.*, A spectrum of routing strategies for brain networks. *PLoS Comput. Biol.* **15**, 1–24 (2019).

21. C. Seguin, S. Mansour L, O. Sporns, A. Zalesky, F. Calamante, Network communication models narrow the gap between the modular organization of structural and functional brain networks. *Neuroimage* **257**, 119323 (2022).

22. F. Zamani Esfahlani, J. Faskowitz, J. Slack, B. Mišić, R. F. Betzel, Local structure-function relationships in human brain networks across the lifespan. *Nat. Commun.* **13** (2022).

23. E. Estrada, N. Hatano, Communicability in complex networks. *Phys. Rev. E - Stat. Nonlinear, Soft Matter Phys.* **77**, 1–12 (2008).

24. C. Chennubhotla, I. Bahar, Signal propagation in proteins and relation to equilibrium fluctuations. *PLoS Comput. Biol.* **3**, 1716–1726 (2007).

25. U. Von Luxburg, A tutorial on spectral clustering. *Stat. Comput.* **17**, 395–416 (2007).

26. A. K. Chandra, P. Raghavan, W. L. Ruzzo, R. Smolensky, P. Tiwari, Electrical resistance of a graph captures its commute and cover times. 574–586 (1989).

27. C. Chennubhotla, Z. Yang, I. Bahar, Coupling between global dynamics and signal transduction pathways: A mechanism of allostery for chaperonin GroEL. *Mol. Biosyst.* **4**, 287–292 (2008).

28. S. I. Dimitriadis, N. A. Laskaris, A. Tzelepi, G. Economou, Analyzing functional brain connectivity by means of commute times: A new approach and its application to track event-related dynamics. *IEEE Trans. Biomed. Eng.* **59**, 1302–1309 (2012).

29. J. R. Sato, C. M. Sato, M. K. D. C. Silva, C. E. Biazoli, Commute time as a method to explore brain functional connectomes. *Brain Connect.* **9**, 155–161 (2019).

30. B. Fischl, FreeSurfer. *Neuroimage* **62**, 774–781 (2012).

31. E. Garyfallidis, *et al.*, Dipy, a library for the analysis of diffusion MRI data. *Front. Neuroinform.* **8**, 1–17 (2014).

32. K. Dill, R. L. Jernigan, I. Bahar, *Protein actions: Principles and modeling* (Garland Science, 2017).

33. K. Dill, S. Bromberg, *Molecular driving forces: statistical thermodynamics in biology, chemistry, physics, and nanoscience* (Garland Science, 2012).

34. C. Weistuch, *et al.*, Metabolism modulates network synchrony in the aging brain. *Proc. Natl. Acad. Sci. U. S. A.* **118**, 1–7 (2021).

35. R. M. Razban, B. B. Antal, K. A. Dill, L. R. Mujica-Parodi, Brain signaling becomes less integrated and more segregated with age. *Netw. Neurosci.* **in press** (2024).

36. H. R. Wilson, J. D. Cowan, Excitatory and Inhibitory Interactions in Localized Populations of Model Neurons. *Biophys. J.* **12**, 1–24 (1972).

37. P. Sanz-Leon, S. A. Knock, A. Spiegler, V. K. Jirsa, Mathematical framework for large-scale brain network modeling in The Virtual Brain. *Neuroimage* **111**, 385–430 (2015).

38. J. L. Lancaster, *et al.*, Automated Talairach atlas labels for functional brain mapping. *Hum. Brain Mapp.* **10**, 120–131 (2000).

39. S. Mansour L., M. A. Di Biase, R. E. Smith, A. Zalesky, C. Seguin, Connectomes for 40,000 UK Biobank participants: A multi-modal, multi-scale brain network resource. *Neuroimage* **283**, 120407 (2023).

40. D. C. Van Essen, *et al.*, The Human Connectome Project: A data acquisition perspective. *Neuroimage* **62**, 2222–2231 (2012).

41. World Health Organization, *ICD-10: international statistical classification of diseases and related health problems: tenth revision* (World Health Organization, 2004).

42. H. Aerts, W. Fias, K. Caeyenberghs, D. Marinazzo, Brain networks under attack: Robustness properties and the impact of lesions. *Brain* **139**, 3063–3083 (2016).

43. N. A. Crossley, *et al.*, The hubs of the human connectome are generally implicated in the anatomy of brain disorders. *Brain* **137**, 2382–2395 (2014).

44. K. G. Schilling, *et al.*, Challenges in diffusion MRI tractography – Lessons learned from international benchmark competitions. *Magn. Reson. Imaging* **57**, 194–209 (2019).

45. C. Thomas, *et al.*, Anatomical accuracy of brain connections derived from diffusion MRI tractography is inherently limited. *Proc. Natl. Acad. Sci. U. S. A.* **111**, 16574–16579 (2014).

46. B. Mišić, *et al.*, The functional connectivity landscape of the human brain. *PLoS One* **9** (2014).

47. K. Shen, *et al.*, Stable long-range interhemispheric coordination is supported by direct anatomical projections. *Proc. Natl. Acad. Sci. U. S. A.* **112**, 6473–6478 (2015).

48. R. A. I. Bethlehem, *et al.*, Brain charts for the human lifespan. *Nature* (2022) https:/doi.org/10.1038/s41586-022-04554-y.

49. S. Barnett, *Matrices: methods and applications* (Oxford University Press, 1990).

50. T. N. E. Greville, Some Applications of the Pseudoinverse of a Matrix. *SIAM Rev.* **2**, 15–22 (1960).

51. C. Chennubhotla, A. J. Rader, L. W. Yang, I. Bahar, Elastic network models for understanding biomolecular machinery: From enzymes to supramolecular assemblies. *Phys. Biol.* **2** (2005).

52. I. Bahar, A. R. Atilgan, B. Erman, Direct evaluation of thermal fluctuations in proteins using a single-parameter harmonic potential. *Fold. Des.* **2**, 173–181 (1997).

53. D. J. Klein, M. Randić, Resistance distance. *J. Math. Chem.* **12**, 81–95 (1993).

54. W. Xiao, I. Gutman, Resistance distance and Laplacian spectrum. *Theor. Chem. Acc.* **110**, 284–289 (2003).

55. J. J. Crofts, D. J. Higham, A weighted communicability measure applied to complex brain networks. *J. R. Soc. Interface* **6**, 411–414 (2009).

56. C. Seguin, Y. Tian, A. Zalesky, Network communication models improve the behavioral and functional predictive utility of the human structural connectome. *Netw. Neurosci.* **4**, 980–1006 (2020).

57. M. Rosvall, A. Grönlund, P. Minnhagen, K. Sneppen, Searchability of networks. *Phys. Rev. E - Stat. Nonlinear, Soft Matter Phys.* **72**, 1–8 (2005).

58. M. Rubinov, O. Sporns, Complex network measures of brain connectivity: Uses and interpretations. *Neuroimage* **52**, 1059–1069 (2010).

59. N. Metropolis, A. W. Rosenbluth, M. N. Rosenbluth, A. H. Teller, E. Teller, Equation of state calculations by fast computing machines. *J. Chem. Phys.* **21**, 1087–1092 (1953).

60. K. J. Friston, A. Mechelli, R. Turner, C. J. Price, Nonlinear responses in fMRI: The balloon model, Volterra kernels, and other hemodynamics. *Neuroimage* **12**, 466–477 (2000).

61. C. Sudlow, *et al.*, UK Biobank: An open access resource for identifying the causes of a wide range of complex diseases of middle and old age. *PLoS Med.* **12**, 1–10 (2015).

62. I. Aganj, *et al.*, Reconstruction of the orientation distribution function in single- and multiple-shell q-ball imaging within constant solid angle. *Magn. Reson. Med.* **64**, 554–566 (2010).

63. R. M. Razban, J. A. Pachter, K. A. Dill, L. R. Mujica-Parodi, Early path dominance as a principle for neurodevelopment. *Proc. Natl. Acad. Sci. U. S. A.* **120**, 1–8 (2023).

64. M. F. Glasser, *et al.*, The minimal preprocessing pipelines for the Human Connectome Project. *Neuroimage* **80**, 105–124 (2013).

65. J. L. R. Andersson, S. N. Sotiropoulos, An integrated approach to correction for off-resonance effects and subject movement in diffusion MR imaging. *Neuroimage* **125**, 1063–1078 (2016).

66. F. Alfaro-Almagro, *et al.*, Image processing and quality control for the first 10,000 brain imaging datasets from UK Biobank. *Neuroimage* **166**, 400–424 (2018).

67. R. Kötter, Online retrieval, processing, and visualization of primate connectivity data from the CoCoMac database. *Neuroinformatics* **2**, 127–144 (2004).

68. R. Kötter, E. Wanke, Mapping brains without coordinates. *Philos. Trans. R. Soc. B Biol. Sci.* **360**, 751–766 (2005).

69. M. F. Glasser, *et al.*, A multi-modal parcellation of human cerebral cortex. *Nature* **536**, 171–178 (2016).

Supplementary Information

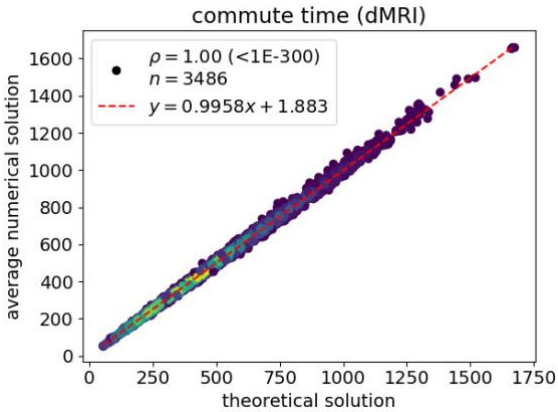

Figure S1: The theoretical expression for commute time (Equation 5) matches numerical results. Commute time is calculated and simulated for a dMRI-derived structure from an arbitrary UK Biobank individual (subject id: 1000366) under the Desikan-Killiany atlas (84 brain regions). We run 1,000 replicate simulations for each pair of brain regions and take its mean to compare with the

theoretical solution. Data points correspond to all possible pairs of brain regions (n = 84x83/2) and are colored to capture the density of points, with brighter colors corresponding to greater density. The symbol ρ corresponds to the Spearman correlation coefficient with its p-value following in parenthesis. The dashed red-line corresponds to the best-fit line. The equation is written in the legend such that y corresponds to the average numerical solution; x corresponds to the theoretical solution.

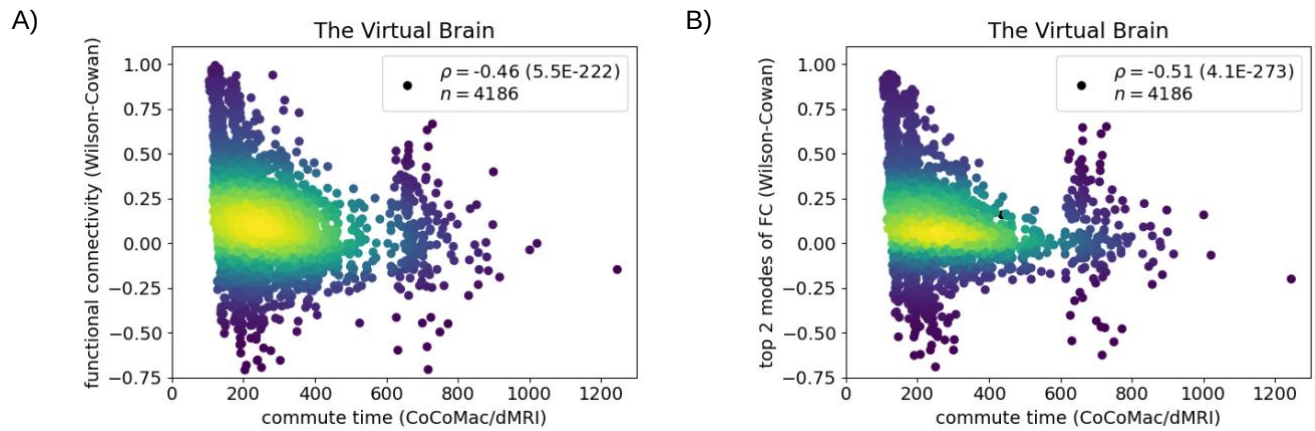

Figure S2: Commute time captures functional connectivity in a Wilson-Cowan simulation. The Wilson-Cowan simulation is run on connectivity data merged from the macaque brain (CoCoMac (67, 68)*) and dMRI provided by The Virtual Brain* (37)*. Parameter values can be found in Table S1 and were chosen such that most neuronal regions demonstrate stable oscillatory dynamics. Data points correspond to all possible pairs of brain regions and are colored to capture the density of points, with brighter colors corresponding to greater density. The same simulation is presented in both A) and B); the difference is that only the top two modes of the functional connectivity matrix is presented in B). For visual clarity, the x-axes are cutoff at a commute time value of 1300, however, there are a cluster of commute times at 4750 and they are included in correlation calculations and n.*

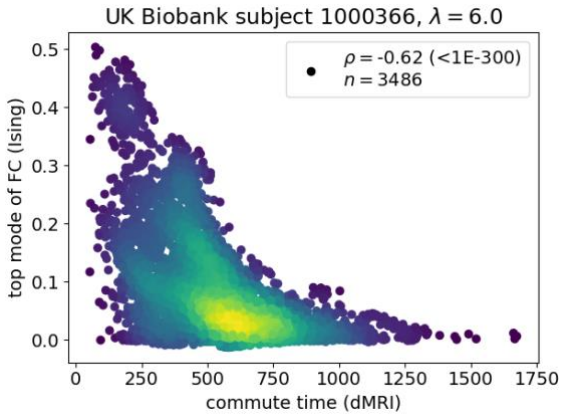

Figure S3: The top mode of the functional connectivity (FC) matrix from an Ising simulation does a poorer job at correlating with commute compared to including all FC modes (Figure 2A). The Ising simulation is the same as that presented in Figure 2.

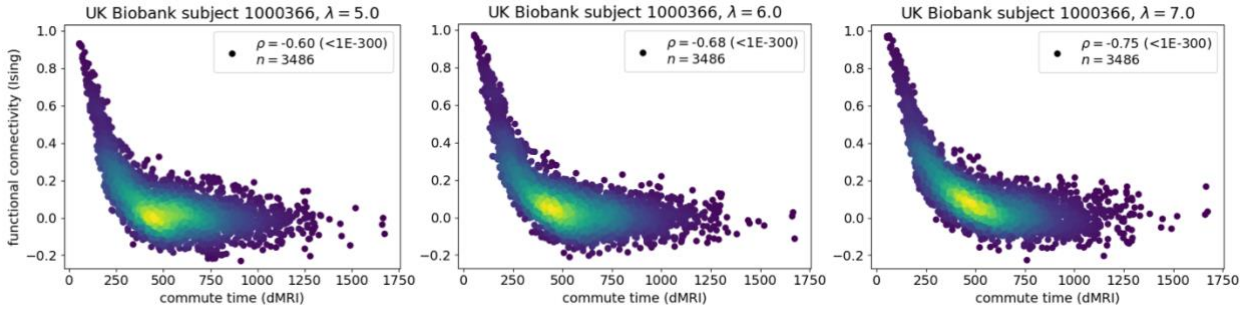

Figure S4: The commute time-functional connectivity correlation is mediated by the Ising model's coupling strength λ. Three different Ising simulations are run on a dMRI-derived structure from the same UK Biobank individual (subject id: 1000366) for three different coupling strength values. The middle plot (λ = 6.0) is also displayed in Figure 2A.

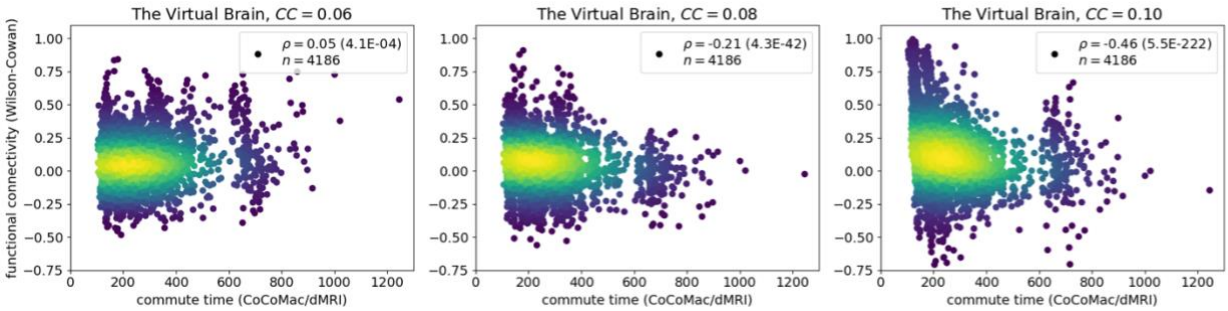

Figure S5: The commute time-functional connectivity correlation is mediated by the Wilson-Cowan model's global coupling constant (CC). All other parameter values are the same as in Figure S2 and can be found in Table S1. Three different Wilson-Cowan simulations are run on connectivity data merged from the macaque brain (CoCoMac (67, 68)*) and dMRI provided by The Virtual Brain* (37) *for three different coupling constant values. For visual clarity, the x-axes are cutoff at a commute time value of 1300, however, there are a cluster of commute times at 4750 and they are included in correlation calculations and n. The right plot (CC = 0.10) is also displayed in Figure S2A.*

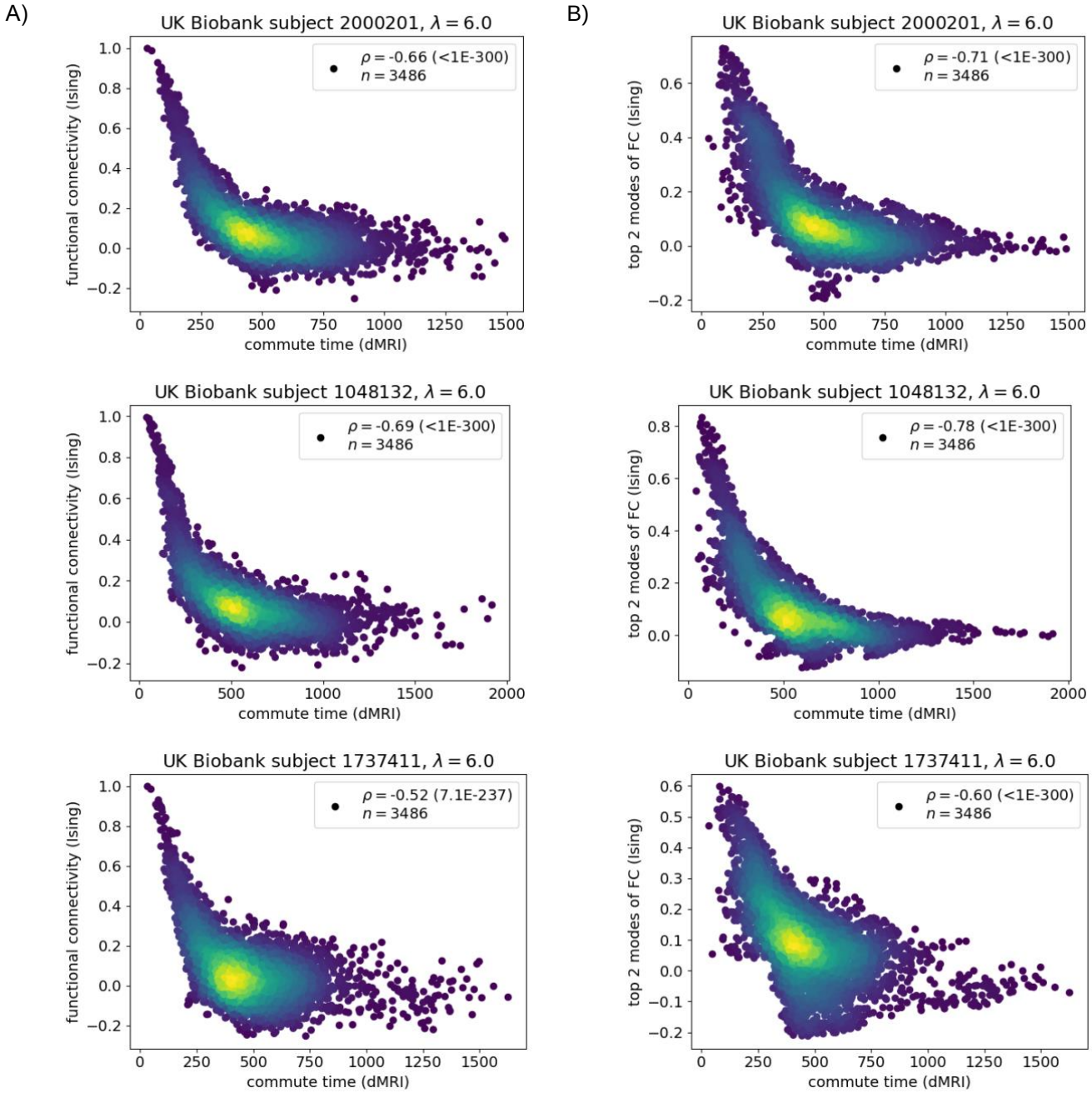

Figure S6: Commute time captures functional connectivity in mean-field Ising simulations for different individuals' structures. The same simulation is presented in each row of A) and B); the difference is that only the top two modes of the functional connectivity (FC) matrix is presented in B). Three sets of Ising simulations are run on a dMRI-derived structure from three different UK Biobank individual (subject id: 2000201, 1048132, 1737411) under the Desikan-Killiany atlas (84 brain regions). The same global coupling strength parameter λ = 6.0 is employed for all individuals (Methods).

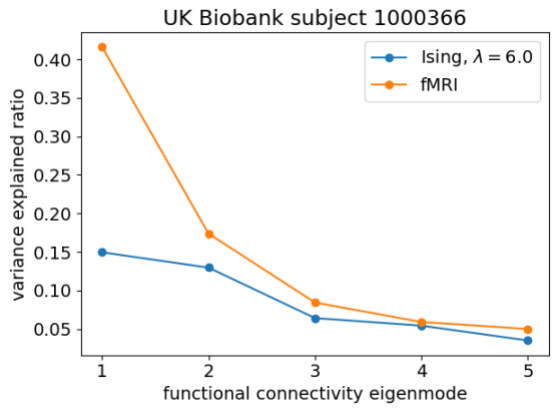

Figure S7: The functional connectivity (FC) matrix derived from fMRI data has a more dominant largest eigenvalue compared to that derived from the Ising simulation with a coupling strength parameter λ = 6.0 on the same individual's dMRI structure (subject id: 1000366) under the Desikan-Killiany atlas (84 brain regions). FCs are the same as those presented in Figure 2A and in Figure 3A, respectively.

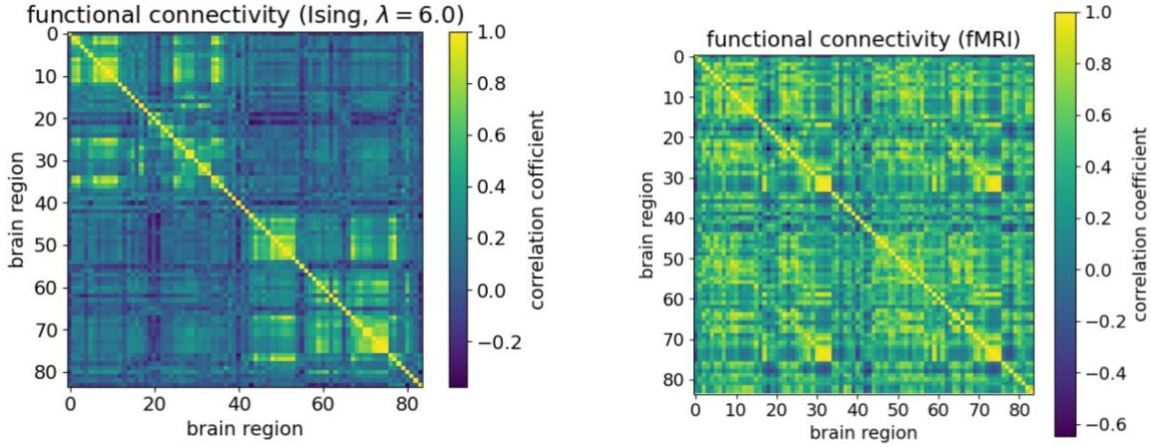

Figure S8: The functional connectivity (FC) matrix derived from the Ising simulation with a coupling strength parameter λ = 6.0 on a UK Biobank individual's dMRI structure (subject id: 1000366) under the Desikan-Killiany atlas (left map) looks qualitatively different than that of the FC matrix derived from fMRI data on the same individual under the same atlas (right map, also shown in Figure 1).

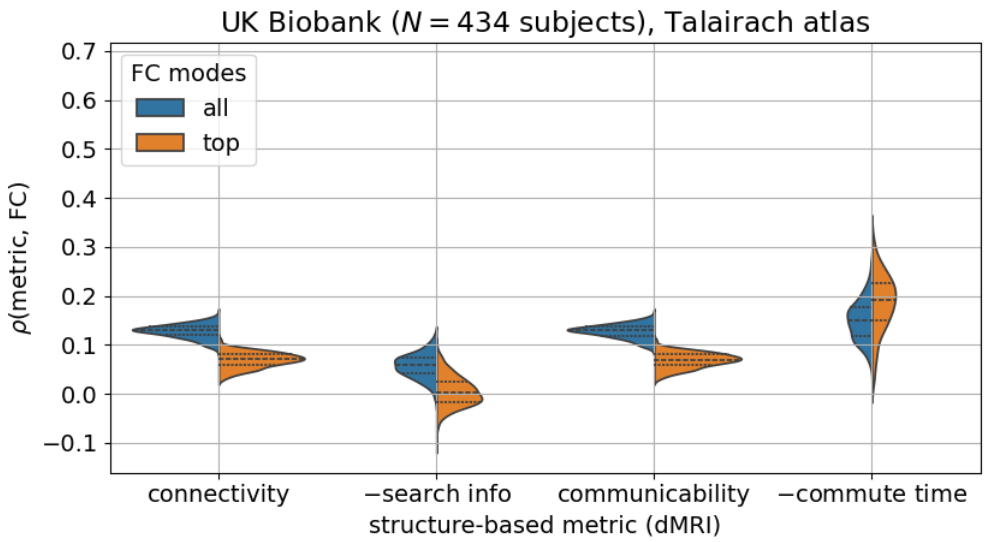

Figure S9: Commute time outperforms other structure-based metrics at predicting functional connectivities regardless of the brain atlas. fMRI and dMRI data are processed according to the Talairach atlas (727 brain regions on average (Methods)). Corresponding Kolmogorov-Smirnov pairwise tests between metrics are summarized in Table S5.

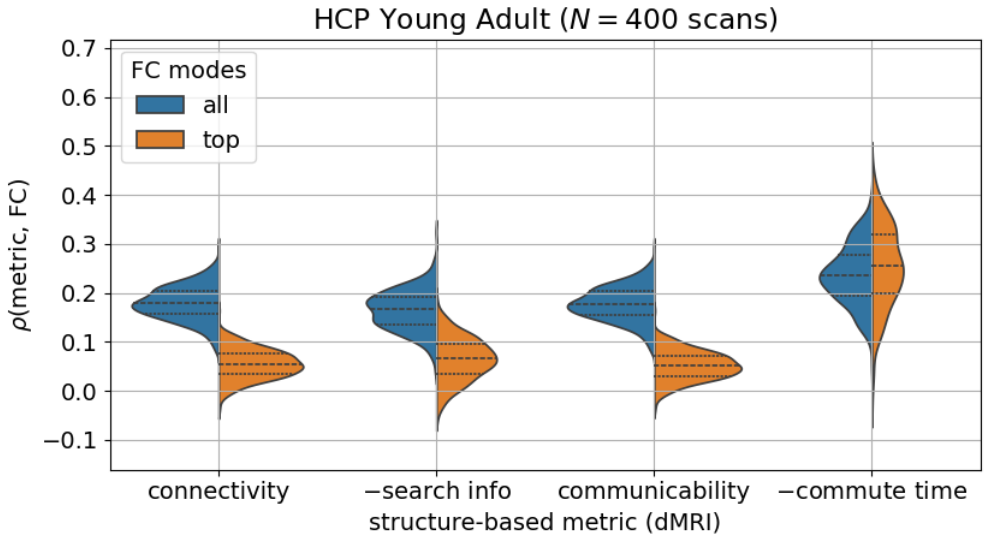

Figure S10: Commute time outperforms other structure-based metrics at predicting functional connectivities (FCs) for the Human Connectome Project (HCP) Young Adult dataset. N corresponds to the number of brain scans considered from HCP Young Adult. Each subject had 4 brain scans and we consider individuals from the 100 Unrelated Subjects subset. fMRI and dMRI data are processed according to the Desikan-Killiany atlas.

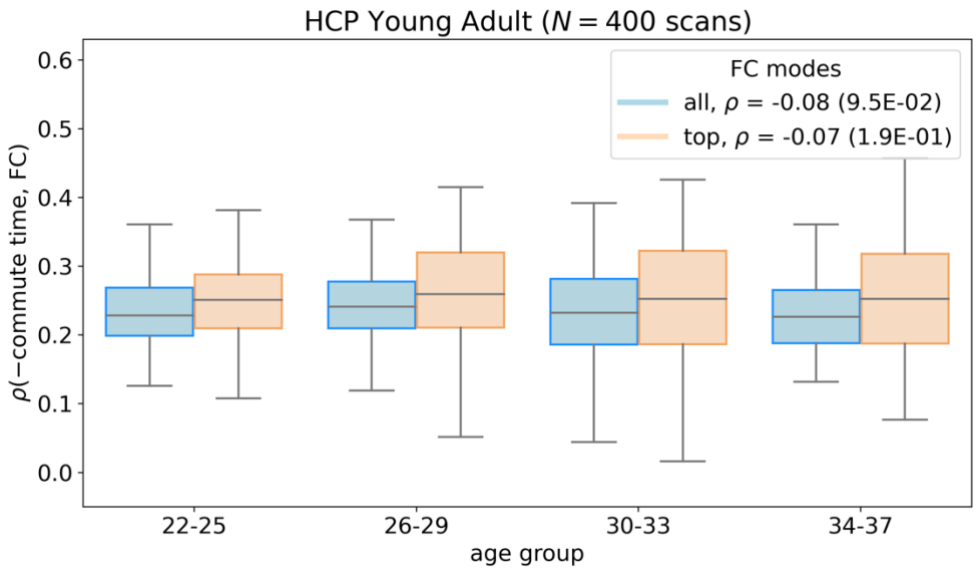

Figure S11: Minimal differences are seen between brain scans from different age groups in the HCP Young Adult dataset. For each group, two distributions are plotted, where the orange distribution only includes the top mode of the FC matrix. fMRI and dMRI data are processed according to the Desikan-Killiany atlas. The symbol ρ corresponds to the Spearman correlation coefficient with its p-value in parenthesis, calculated for all data points.

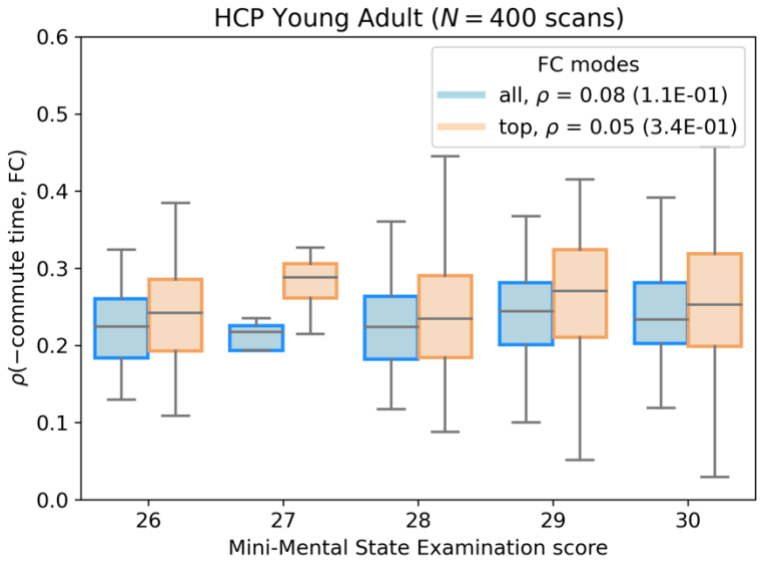

Figure S12: Minimal differences are seen between brain scans from individuals with different Mini-Mental State Examination scores in the HCP Young Adult dataset. fMRI and dMRI data are processed according to the Desikan-Killiany atlas.

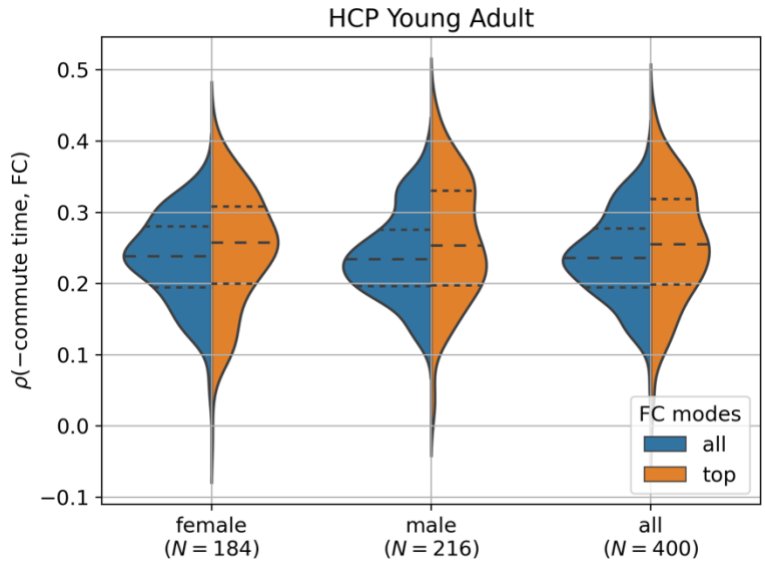

Figure S13: Minimal differences are seen between brain scans from different sexes in the HCP Young Adult dataset. N corresponds to the number of brain scans considered for that particular group from the HCP Young Adult. fMRI and dMRI data are processed according to the Desikan-Killiany atlas.

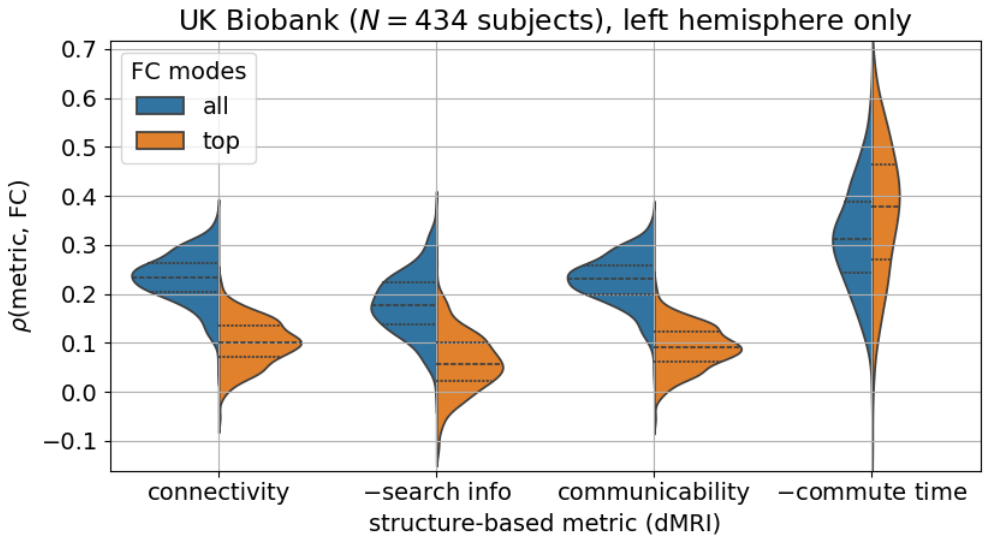

Figure S14: Commute time outperforms other structure-based metrics at predicting functional connectivities (FCs), even when only analyzing intra-hemisphere connections from the left hemisphere. Corresponding Kolmogorov-Smirnov pairwise tests between metrics are summarized in Table S6. fMRI and dMRI data are processed according to the Desikan-Killiany atlas.

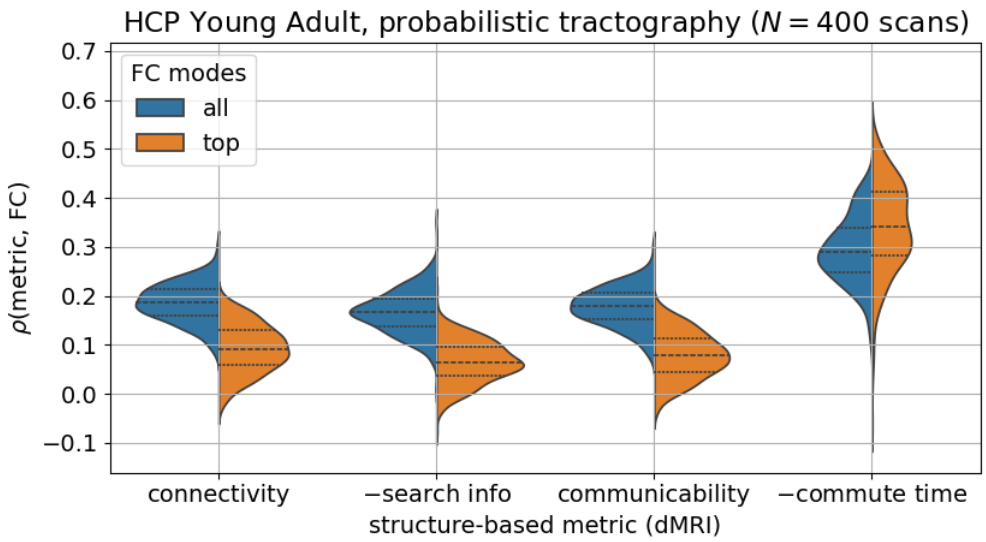

Figure S15: Commute time outperforms other structure-based metrics at predicting functional connectivities (FCs), even when analyzing connections derived from probabilistic tractography. fMRI and dMRI data are processed according to the Desikan-Killiany atlas.

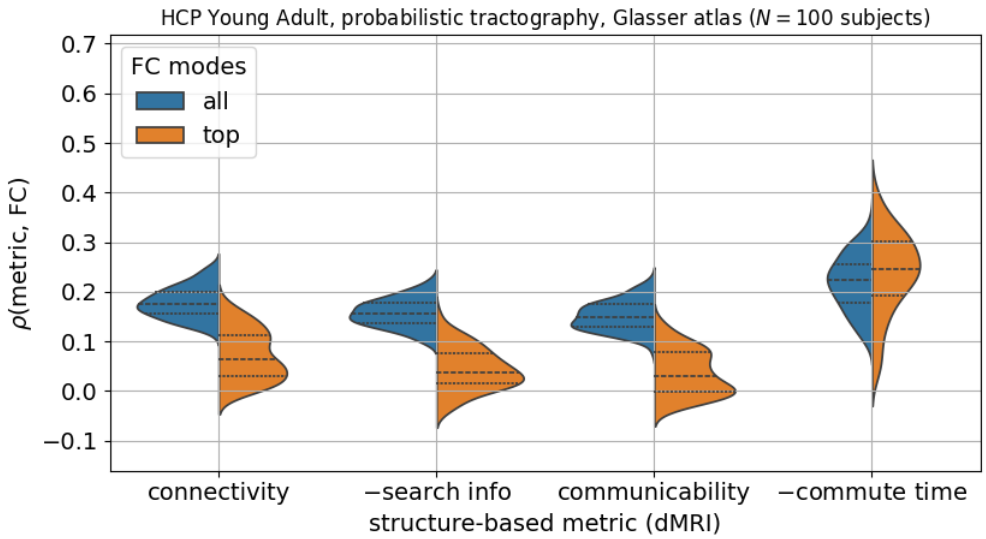

Figure S16: Commute time outperforms other structure-based metrics at predicting functional connectivities (FCs), even when analyzing connections derived from probabilistic tractography from another study (14)*. N corresponds to the number of subjects considered from HCP Young Adult 100 Unrelated Subjects subset. Each subject had 4 brain scans which were concatenated into one large scan. fMRI and dMRI data are processed according to the Glasser atlas* (69) *(360 brain regions). Probabilistic tractography was performed and publicly provided by Rosen et al.* (14)*.*

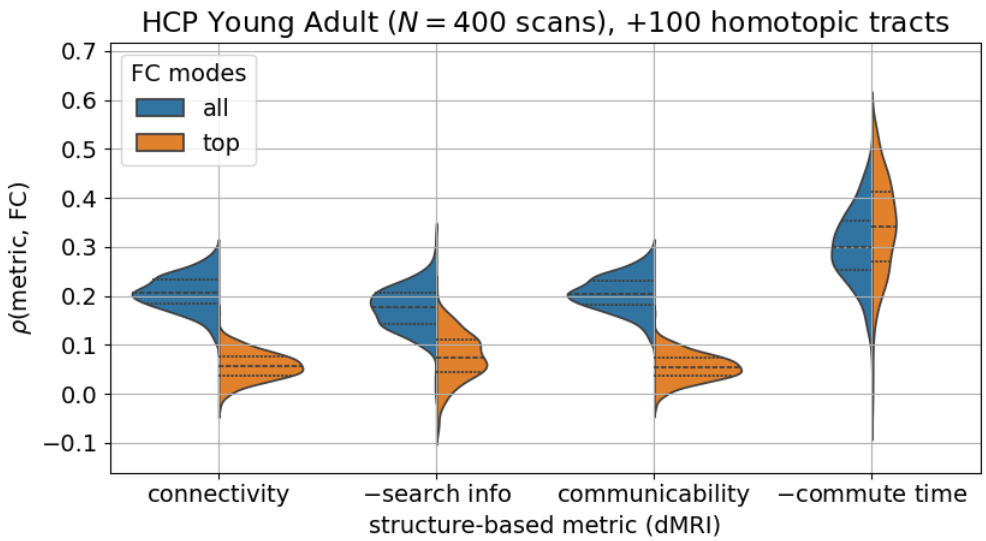

Figure S17: Commute time outperforms other structure-based metrics at predicting FCs, even when manually adding 100 homotopic connections per region. fMRI and dMRI data are processed according to the Desikan-Killiany atlas.

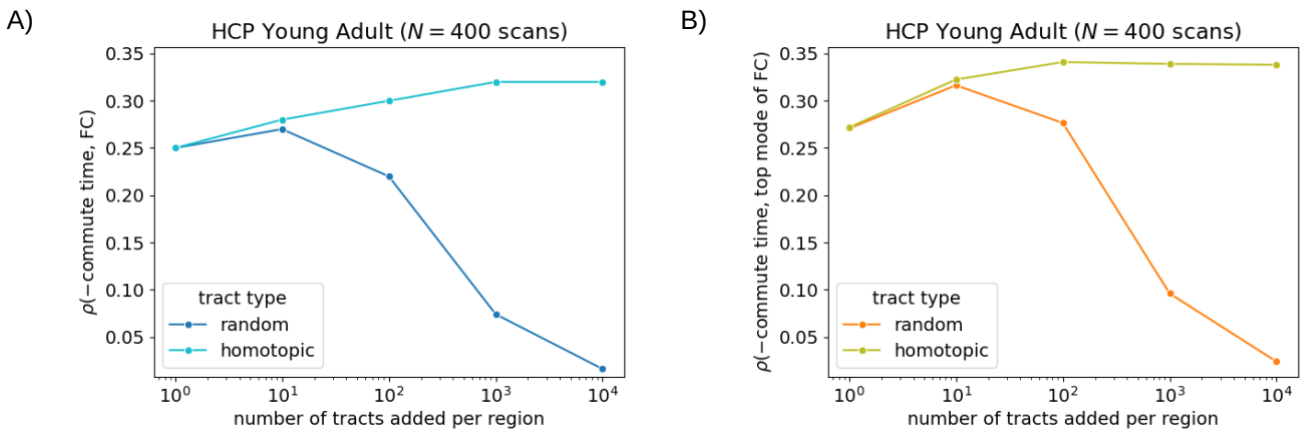

Figure S18: White matter tracts added between homotopic regions improve the average commute time-FC correlation, especially compared to randomly added connections. The full distribution across all HCP Young Adult brain scans from the 100 Unrelated Subjects subset is shown for 100 added homotopic connections in Figure S17. Assessments are made for every order of magnitude up to 10,000 added white matter tracts. The entirety of the FC is considered in A). Only the top mode of the FC matrix is considered in B). fMRI and dMRI data are processed according to the Desikan-Killiany atlas.

Parameter	Description	Value
	Population time constants	
r_e	Excitatory refractory period [ms]	1 ms
r_i	Inhibitory refractory period [ms]	1 ms

k_e	Maximum value of the excitatory response function	1
k_i	Maximum value of the inhibitory response function	1
τ_e	Excitatory population, membrane time-constant [ms]	8 ms
τ_i	Inhibitory population, membrane time-constant [ms]	8 ms
Local network connectivity parameters		
c_{ee}	Excitatory to excitatory coupling coefficient	15.8
c_{ei}	Inhibitory to excitatory coupling coefficient	15.6
c_{ie}	Excitatory to inhibitory coupling coefficient	30
c_{ii}	Inhibitory to inhibitory coupling coefficient	6
α_e	Balance parameter between excitatory and inhibitory masses	1
α_i	Balance parameter between excitatory and inhibitory masses	1
Activation function parameters		
a_e	The slope parameter for the excitatory response function	1
a_i	The slope parameter for the inhibitory response function	1
b_e	Position of the maximum slope of the excitatory sigmoid function	0
b_i	Position of the maximum slope of the inhibitory sigmoid function	0
c_e	The amplitude parameter for the excitatory response function	1
c_i	The amplitude parameter for the inhibitory response function	1
ϑ_e	Excitatory threshold	0
ϑ_i	Inhibitory threshold	0

External perturbation parameters		
P	External stimulus to the excitatory population	-3.575
Q	External stimulus to the inhibitory population	-7.4
Global Connectivity parameters		
CV	Conduction velocity between brain regions	3.0
CC	Coupling constant between brain regions	0.1

Table S1: Wilson-Cowan model parameter descriptions and values for Figure S2. Descriptions are adapted from Tables 10 and 11 of Sanz-Leon et al. (37).

KS \\ p-value	**connectivity**	**search info**	**communicability**	**commute time**
connectivity	\\	1.0E-11 | 3.1E-31	0.11 | 0.21	2.2E-59 | 2.2E-59
search info	0.50 | 0.79	\\	3.4E-13 | 3.9E-33	2.6E-44 | 4.4E-55
communicability	0.17 | 0.15	0.53 | 0.81	\\	2.2E-59 | 2.2E-59
commute time	1.0 | 1.0	0.91 | 0.98	1.0 | 1.0	\\

Table S2: Summary statistics of Kolmogorov-Smirnov (KS) pairwise tests for distributions presented in Figure 2C when including all modes (left of the vertical line \|) and only the top mode (right of \|) of the functional connectivity matrix from Ising simulations on UK Biobank (subject id: 1000366) with a coupling strength parameter λ = 6. KS test statistics are entered in the bottom left of the table; corresponding p-values are in the top right.

KS \\ p-value	**connectivity**	**search info**	**communicability**	**commute time**
connectivity	\\	4.0E-18 | 5.1E-07	0.89 | 0.33	2.3E-70 | 1.1E-216
search info	0.30 | 0.19	\\	5.2E-16 | 2.4E-5	2.6E-84 | 3.3E-203
communicability	0.040 | 0.065	0.29 | 0.16	\\	1.5E-71 | 2.9E-218
commute time	0.59 | 0.95	0.64 | 0.93	0.59 | 0.95	\\

Table S3: Summary statistics of Kolmogorov-Smirnov (KS) pairwise tests for distributions presented in Figure 3C when including all modes (left of the vertical line \|) and only the top mode (right of \|) of the functional connectivity matrix from fMRI data of

434 UK Biobank individuals. KS test statistics are entered in the bottom left of the table; corresponding p-values are in the top right.

KS \\ p-value	mental disorder	brain disease	healthy
mental disorder	\\	0.15 | 0.35	0.12 | 0.27
brain disease	0.6 | 0.48	\\	0.78 | 0.32
healthy	0.55 | 0.46	0.16 | 0.24	\\

Table S4: Summary statistics of Kolmogorov-Smirnov (KS) pairwise tests for distributions presented in Figure 4A when including all modes (left of the vertical line \|) and only the top mode (right of \|) of the functional connectivity matrix from fMRI data of 434 UK Biobank individuals. KS test statistics are entered in the bottom left of the table; corresponding p-values are in the top right.

KS \\ p-value	connectivity	search info	communicability	commute time
connectivity	\\	3.3E-203 | 1.2E-152	1.0 | 1.0	2.9E-43 | 1.7E-184
search info	0.93 | 0.83	\\	1.2E-204 | 1.3E-151	8.5E-168 | 4.4E-206
communicability	0.014 | 0.028	0.93 | 0.83	\\	2.9E-43 | 1.7E-184
commute time	0.47 | 0.90	0.86 | 0.93	0.47 | 0.90	\\

Table S5: Summary statistics of Kolmogorov-Smirnov (KS) pairwise tests for distributions presented in Figure S9 when including all modes (left of the vertical line \|) and only the top mode (right of \|) of the functional connectivity matrix from fMRI data under the Talairach atlas of 434 UK Biobank individuals. KS test statistics are entered in the bottom left of the table; corresponding p-values are in the top right.

KS \\ p-value	connectivity	search info	communicability	commute time
connectivity	\\	1.1E-32 | 1.5E-21	0.47 | 0.0098	1.7E-45 | 1.4E-173
search info	0.41 | 0.33	\\	5.5E-28 | 2.9E-16	2.8E-78 | 6.2E-176
communicability	0.058 | 0.11	0.38 | 0.29	\\	2.9E-48 | 3.0E-183
commute time	0.48 | 0.88	0.62 | 0.88	0.49 | 0.89	\\

Table S6: Summary statistics of Kolmogorov-Smirnov (KS) pairwise tests for distributions presented in Figure S14 when including all modes (left of the vertical line |) and only the top mode (right of |) of the functional connectivity matrix from fMRI data for only left hemisphere regions of 434 UK Biobank individuals. KS test statistics are entered in the bottom left of the table; corresponding p-values are in the top right.

Data set	age range	<age>± std(age)	sex
UK Biobank	46-79	62.6 ± 7.4	232F / 202M
HCP Young Adult	22-36	29.1 ± 3.7	184F / 216M

Table S7: Demographic information of the individuals considered in this paper. Ages are in units of years.

Data set	field strength	repetition time	echo time	flip angle	voxel size	total time points
UK Biobank	3T	735 ms	39 ms	52°	2.4x2.4x2.4 mm^3	490
HCP Young Adult	3T	720 ms	33.1 ms	52°	2x2x2 mm^3	1200

Table S8: Functional MRI acquisition parameters of the data sets.

Commute time derivation

We expand upon the Methods derivation by showing how applying Greville's formula twice takes us from Equation 9 and Equation 10. If $\boldsymbol{A}_k$ is a *m* x *k* matrix, Greville's formula states that the generalized matrix of $\boldsymbol{A}_k$ by appending an additional column a_{k+1} ($\boldsymbol{A}_{k+1}^{+}$) can be expressed as (49, 50),

Equation 14

$$\boldsymbol{A}_{k+1}^{+} = [\boldsymbol{A}_k, a_{k+1}]^{+} = \begin{bmatrix} \boldsymbol{A}_k^{+} - d_k b_k \\ b_k \end{bmatrix}$$

The symbols d_k and b_k are defined as,

Equation 15

$$d_k = \boldsymbol{A}_k^{+} a_{k+1},\ c_k = a_{k+1} - \boldsymbol{A}_k d_k$$
$$b_k = \begin{cases} c_k^T, & \text{if } c_k \neq 0 \\ (1 + d_k^T d_k)^{-1} d_k^T \boldsymbol{A}_k^{+}, & \text{if } c_k = 0 \end{cases}$$

With Greville's formula, we can express $\widehat{\boldsymbol{\Gamma}}^{-1}$ in terms of $\boldsymbol{\Gamma}^{-1}$ as follows. First, we define $\widetilde{\boldsymbol{\Gamma}}$ as an (*n*-1) x *n* matrix.

Equation 16

$$\boldsymbol{\Gamma} = \begin{bmatrix} \widetilde{\boldsymbol{\Gamma}} \\ r^T \end{bmatrix}$$

It can be shown that the row vector $r^T = -\widehat{\mathbf{1}}^T\widetilde{\boldsymbol{\Gamma}}$ to ensure the condition that the sum of rows of the Laplacian matrix must be equation to $\mathbf{1}^T\boldsymbol{\Gamma} = \mathbf{0}$.
To connect $\widetilde{\boldsymbol{\Gamma}}$ to $\widehat{\boldsymbol{\Gamma}}$, we have the following relationship:
Equation 17

$$\widetilde{\boldsymbol{\Gamma}} = [\widehat{\boldsymbol{\Gamma}}, s]$$

It can be shown that the vector $s = -\widehat{\mathbf{1}}^T\widetilde{\boldsymbol{\Gamma}}$ to ensure the condition that sum of columns of the Laplacian matrix must be equal to 0 ($\boldsymbol{\Gamma}\mathbf{1} = \mathbf{0}^T$).

We are now ready to apply Greville's formula. We can calculate the pseudoinverse of $\widetilde{\boldsymbol{\Gamma}}$,
Equation 18

$$\widetilde{\boldsymbol{\Gamma}}^{-1} = \begin{bmatrix} \widehat{\boldsymbol{\Gamma}}^{-1} + \widehat{\mathbf{1}}b_k \\ b_k \end{bmatrix}$$

We do not need to directly evaluate b_k from Equation 15. Instead, we can notice that b_k must be equal to the removed j^{th} row in $\widehat{\boldsymbol{\Gamma}}$ that is present in $\widetilde{\boldsymbol{\Gamma}}$.
Equation 19

$$\widetilde{\boldsymbol{\Gamma}}^{-1} = \begin{bmatrix} \widehat{\boldsymbol{\Gamma}}^{-1} \\ 0 \end{bmatrix} + \begin{bmatrix} \widehat{\mathbf{1}}b_k \\ b_k \end{bmatrix}$$
$$\rightarrow b_k = \left[\widetilde{\boldsymbol{\Gamma}}^{-1}\right]_j$$

In component form, Equation 19 is equivalent to:
Equation 20

$$\left[\widetilde{\boldsymbol{\Gamma}}^{-1}\right]_{lm} = \left[\widehat{\boldsymbol{\Gamma}}^{-1}\right]_{lm} + \left[\widetilde{\boldsymbol{\Gamma}}^{-1}\right]_{jm}$$
$$\rightarrow \left[\widehat{\boldsymbol{\Gamma}}^{-1}\right]_{lm} = \left[\widetilde{\boldsymbol{\Gamma}}^{-1}\right]_{lm} - \left[\widetilde{\boldsymbol{\Gamma}}^{-1}\right]_{jm}$$

We can perform the same steps as in Equation 18 and Equation 19 to express $\widetilde{\boldsymbol{\Gamma}}^{-1}$ in terms of $\boldsymbol{\Gamma}^{-1}$,
Equation 21

$$\left[\widetilde{\boldsymbol{\Gamma}}^{-1}\right]_{no} = [\boldsymbol{\Gamma}^{-1}]_{no} - [\boldsymbol{\Gamma}^{-1}]_{jn}$$

Inserting Equation 21 into Equation 20, we finally have our expression for $\widehat{\boldsymbol{\Gamma}}^{-1}$ in terms of $\boldsymbol{\Gamma}^{-1}$.
Equation 22

$$\left[\widehat{\boldsymbol{\Gamma}}^{-1}\right]_{lm} = [\boldsymbol{\Gamma}^{-1}]_{lm} - [\boldsymbol{\Gamma}^{-1}]_{jl} - [\boldsymbol{\Gamma}^{-1}]_{jn} + [\boldsymbol{\Gamma}^{-1}]_{jj}$$

Equation 22 can be inserted in Equation 9 to obtain Equation 10.